Chinese Chemical Letters 36 (2025) 110132

Contents lists available at ScienceDirect

Chinese Chemical Letters

journal homepage: www.elsevier.com/locate/cclet

A label-free and ratiometric fluorescent sensor based on porphyrin-metal-organic frameworks for sensitive detection of ochratoxin A in cereal

Yijian Zhao, Jvzhe Li, Yunyi Shi, Jie Hu, Meiyi Liu, Yao Shen, Xinglin Hou, Qiuyue Wang, Qi Wang, Zhiyi Yao*

Beijing Laboratory of Food Quality and Safety, College of Food Science and Nutritional Engineering, China Agricultural University, Beijing 100083, China

ARTICLE INFO

Article history:
Received 22 February 2024
Revised 29 May 2024
Accepted 14 June 2024
Available online 16 June 2024

Keywords:
Ochratoxin A
Porphyrinic metal-organic framework
Silica nanoparticle
Ratiometric fluorescent sensing
Food safety

ABSTRACT

The fabrication of bioreceptor-free method for accurate and sensitive detection of ochratoxin A (OTA) in cereal is critical, but still a significant challenge to mitigate risks to food industries and public health. In this study, a smartphone-ratiometric fluorescence sensor for the ultrasensitive detection of OTA is developed based on a porphyrinic metal-organic framework and silica nanoparticle composite (Zr-MOF/SiNPs) away from the use of antibodies and aptamers. Due to the excellent recognition ability of Zr-MOF and good storage stability of SiNPs, OTA is detected by Zr-MOF/SiNPs with a wide linear range of 0.05–1000 ng/mL and low detection limit of 0.016 ng/mL. Moreover, the red–blue ratio values of the fluorescence images are extracted through the smartphone color recognizer application with a limit of detection of 1.74 ng/mL, lower than the permissible content of OTA in cereal prescribed by World Health Organization. This sensing platform has been successfully applied in maize samples with superior repeatability and satisfactory recoveries, providing a novel way for simple and label-free analysis of OTA in cereal.

Ochratoxin A (OTA), as one of the most toxic mycotoxins worldwide, exhibits a prominent threat on livestock health owing to its strong nephrotoxicity, teratogenic, carcinogenic, and immunosuppressive effects [1–3]. Due to its thermal and chemical stability, OTA was prevalently monitored in a wide variety of foodstuffs such as corn, cereals, and wheat [4,5]. Given by this, its maximum residue in grains is 5 μg/kg regulated by the European Union (EU) and China [6,7]. Therefore, a highly sensitive and rapid method for detecting OTA in contaminated foodstuffs is essential for food safety as well as public health [8]. Currently, various techniques such as high-performance liquid chromatography (HPLC) [9], enzyme-linked immunosorbent assay (ELISA) [10], surface-enhanced Raman scattering (SERS) [11], fluorescent assay [12], and electrochemical method [13,14] were applied for analysis of OTA with satisfactory accuracy. Although these existing analytical techniques manifest good sensitivity requirements, most of them require professional technology and expensive equipment and involve time-consuming procedures [15–18]. Therefore, developing a facile, time-saving and sensitive method for OTA monitoring in food is of extraordinary practical significance.

Fluorescence sensors have advantages of high sensitivity, low cost, clear signal and dynamic real-time monitoring, which are widely used in the field of analytical sensing [19–22]. Currently, fluorescent detection methods for OTA mainly relies on the natural recognition elements, such as antibodies and aptamers [23–26]. For instance, Guo and coworkers built a ratiometric fluorescent aptasensor for the screening of OTA on-site based on nanomaterials and elegant design strategy for aptamer probes, exhibiting excellent specificity among a variety of mycotoxins [12]. However, the bioreceptors suffer from complex preparation and poor stability, limiting their further use in practical applications [27,28]. Accordingly, it is still a great challenge to develop a direct and label-free fluorescent method without the assistant of bioreceptors for OTA detection. Considering the weak interaction of OTA and fluorescent probes, the design of probe is vital to availably detect the targets [29–32]. A stable and high-performance probe need to meet several conditions: (1) Specific recognition and enrichment ability to OTA from complex conditions, (2) good luminescence properties under visible light excitation, (3) fast response performance for OTA in real samples.

Luminescent metal–organic frameworks (LMOFs) are a kind of ordered porous materials constructed from the self-assembly of metal nodes and organic ligands, which are receiving considerable

* Corresponding author.
E-mail address: yaozy@cau.edu.cn (Z. Yao).

https://doi.org/10.1016/j.cclet.2024.110132
1001-8417/

attention in fluorescence sensing [33–36]. Compared with most of fluorescent probe materials, LMOFs are a promising candidate for OTA analysis with the merits of that a large number of organic linkers can be flexibly designed according to requirements, which contributes to easily distinguishing analytes and interferers through home-guest and functional group interactions [37–39]. Nevertheless, the drawbacks of pure LMOFs, such as single signal readout way, poor water stability and weakly interactions toward mycotoxin, are not be ignored in sensing of OTA molecules [40–42]. In this regard, nanostructured LMOFs possessing strong resistance to water interference, high throughput testing capability and efficient binding ability with target molecules should be designed and fabricated reasonably as well as a good replacement [43–46]. Moreover, it cannot be ignored that the numerous background interferences are also important factors for reducing the sensitivity and accuracy of LMOFs based OTA sensors, which also is an obstacle that limits the quantitative abilities of fluorescence sensors in practical application [47–49]. Therefore, simultaneously improving the sensitivity and reliability of LMOFs based fluorescence sensors applied in aqueous medium is the main challenge for OTA rapid monitoring in practical application.

In this work, an integrated smartphone-ratiometric fluorescent sensing platform based on nanostructured LMOFs (Zr-MOF) and silica nanoparticle (SiNPs) was successfully constructed *via* a facile self-assembly method for rapid, sensitive and reliable detection of OTA in cereal. The nanostructured porphyrinic Zr-MOF with red emission was selected as a highly sensitive recognition unit for OTA due to its large mesopores and a tunable aspect ratio. Also, SiNPs was introduced to the sensing system for enhancing the photostability and water-dispersibility of Zr-MOF, endowing prepared sensor with high reliability and excellent accuracy toward OTA determination. As illustrated in Scheme 1, by addition of OTA, the change of fluorescence color from red to blue was subsequently converted to the red–green–blue (RGB) channel values by smartphone, which contribute to more intuitive results reading and realizing quantitative determination of OTA in cereal samples. Compared with previous OTA sensing systems, our platform exhibits two distinctive features. One is that a straightforward and label-free fluorescent strategy was obtained for rapid detection of OTA rather than the use of bioreceptors. The other is achieving ratiomertic detection based on smart device in practical application. This method will provide novel ideas for the update and replacement of intelligent sensors for efficient monitoring OTA in food.

The morphologies of the prepared Zr-MOF, SiNPs and Zr-MOF/SiNPs were characterized through TEM images. As depicted in Fig. S1A (Supporting information), it can be clearly observed that the Zr-MOF possessed the typical cube shape with an average particle size of ~28 nm. Fig. S1B (Supporting information) showed that the SiNPs had a spherical shape and uniform dispersion with an average diameter of ~60 nm. The average diameter of Zr-MOF/SiNPs increased from 60 nm to 72 nm after the modification of SiNPs, indicating the formation of a more ordered structure Zr-MOF/SiNPs and adopted a more ordered structure (Fig. 1A). The hydrodynamic size of Zr-MOF/SiNPs was 145.6 nm in HEPES buffer based on dynamic light scattering (DLS) measurement, which remain stable among 15 days (Fig. S2 in Supporting information). The loading of SiNPs was determined by inductively coupled plasma (ICP) technique. 4.98 mg Si and 5.99 mg Zr per liter (L) were obtained. Then, the element composition of Zr-MOF/SiNPs were characterized by X-ray photoelectron spectroscopy (XPS). As shown in Fig. 1B, the Zr-MOF/SiNPs is mainly composed of Zr 3d (183.2 eV), Si 2p (101.48 eV), Si 2s (152.48 eV), C 1s (305.48 eV), N 1s (398.48 eV), and O 1s (531.48 eV). In the high-resolution XPS spectrum of Si 2p (Fig. 1C), three fitting peaks at 101.48 eV, 102.18 eV, and 100.98 eV revealed the presence of Si–N, Si–O, and Si–C, respectively. The XPS spectrum of Zr 3d (Fig. 1D) included two fitting peaks, which fitted to Zr $3d_{5/2}$ (182.6 eV), Zr $3d_{3/2}$ (184.8 eV). After coupling SiNPs, the binding energies for Zr 3d show a lower binding energy shift, which indicates a more electron deficiency and higher valence state of Zr^{4+} ions and an intensely denoting electron from O to Zr. Moreover, relatively high peak intensity of Si 2P was observed, which might be assigned to surface oxidation of Si. As presented in infrared spectrum of Zr-MOF (Fig. 1E), the characteristic peaks at 1720, 1601, 1550, and 1415 cm^{-1} correspond to the big ring skeleton absorptions. The signals in the range of 500–700 cm^{-1} can be allocated to asymmetric vibrations of the C=N, N–H, C=C and C–H of the pyrrole ring in TCPP [50]. The absorption peaks of SiNPs at 2929 and 2856 cm^{-1} represented the stretching and bending vibrations of C−H on the saturated carbon, respectively. The characteristic signal at 1090 cm^{-1} was assigned to the extensional vibration of Si−O−Si, while the peak at 910 cm^{-1} belonged to the Si−N stretching vibration. The characteristic peak position of Zr-MOF/SiNPs was accordance with that of the parent MOFs and SiNPs, revealing the SiNPs was attached successfully. The structure of the Zr-MOF/SiNPs was further confirmed by the powder X-ray diffraction (PXRD) patterns [51,52]. In Fig. 1F, concisely matched peaks in small angle sections validated that the crystal structure of Zr-MOF was maintained. The peak emerging at 15°–35° was attributed to the scattering effect of the nanoparticles. Furthermore, the PXRD result of Zr-MOF/SiNPs is still consistent with that of Zr-MOF and the new peaks emerging at 20°–70° shows presence of silica, suggesting the Zr-MOF were attached on the surface of SiNPs.

The optical properties of the Zr-MOF/SiNPs were measured using UV–vis absorption and fluorescence spectra. As shown in Fig. 2A and Fig. S3A (Supporting information), UV–vis spectra of Zr-MOF exhibited a similar pattern of H_4TCPP, which inherited the Soret band at 420 nm and four Q bands at 521, 574, 603, and 656 nm from porphyrin absorption. The redshift of absorption spectra of Zr-MOF was attributed to the enlarged conjugate area of porphyrin after the formation of the Zr-MOFs. The SiNPs showed two absorption peaks at 271 and 362 nm, which could be attributed to the $\pi-\pi^*$ transition and $n-\pi^*$ transition, respectively. As shown in Fig. S3B (Supporting information), H_4TCPP displayed the maximum emission peak at 660 nm, whereas the Zr-MOF had a similar pattern with blue shifting at 650 nm. At an excitation wavelength of 400 nm, the maximum emission peak of Zr-MOF was found at 650 nm (Fig. 2B), and the larger Stokes shift (250 nm) would reduce background interference significantly. The fluorescent (FL) intensity of SiNPs displayed maximum emission peak at 450 nm with an excitation of 375 nm (Fig. 2C). Additionally, the fluorescence lifetime of Zr-MOF and Zr-MOF/SiNPs were estimated to 3.48 ns and 1.74 ns, respectively (Fig. 2D). The fluorescence lifetime will be shortened during FRET, which further reveal the formation of Zr-MOF/SiNPs complex. In Fig. 2E, the emis-

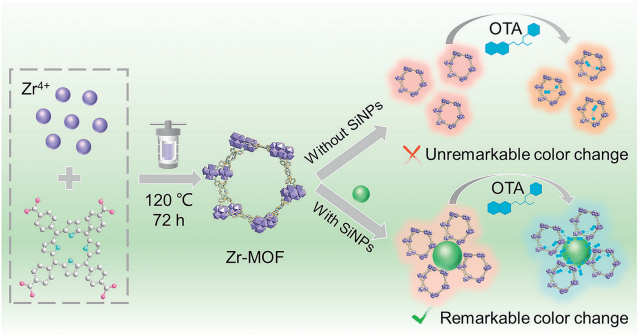

Scheme 1. Schematic illustration of the ratiometric fluorescent probe (Zr-MOF/SiNPs) for OTA detection.

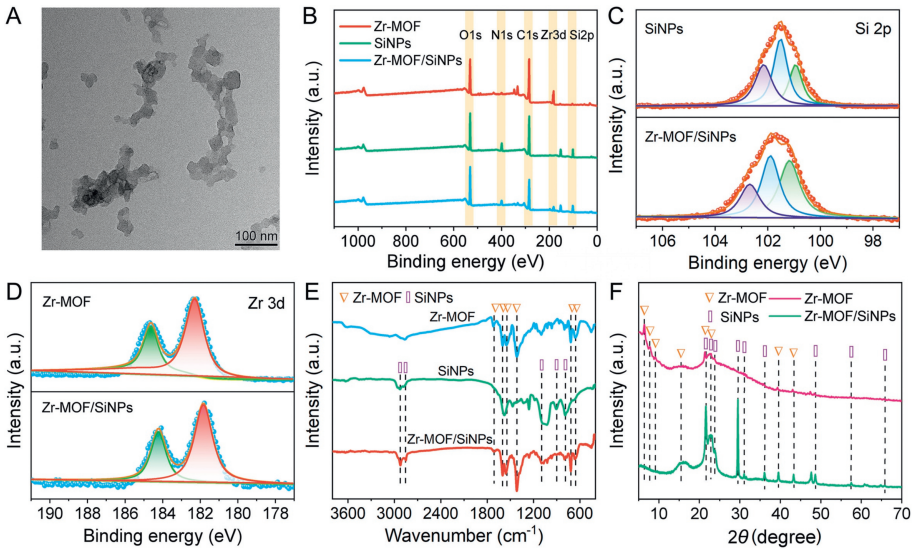

Fig. 1. (A) TEM images of Zr-MOF/SiNPs. (B) XPS survey spectra of Zr-MOF, SiNPs, Zr-MOF/SiNPs. (C) XPS peak fitting scans of the Si 2p of SiNPs and Zr-MOF/SiNPs. (D) XPS spectra of the Zr 3d region of Zr-MOF and Zr-MOF/SiNPs. (E) FTIR spectra of Zr-MOF, SiNPs and Zr-MOF/SiNPs. (F) PXRD patterns of Zr-MOF, and Zr-MOF/SiNPs.

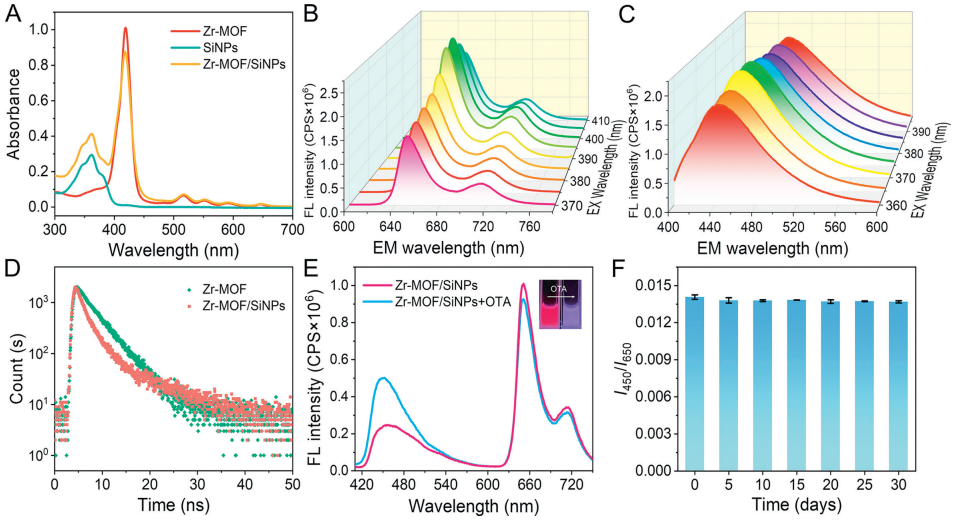

Fig. 2. (A) UV–vis spectra of Zr-MOF, SiNPs and Zr-MOF/SiNPs. (B) Fluorescent spectra of Zr-MOF under different excitation wavelength. (C) Fluorescent spectra of SiNPs under different excitation wavelength. (D) Fluorescence lifetime of Zr-MOF and Zr-MOF/SiNPs at 650 nm (excited at 365 nm). (E) Fluorescent spectra of Zr-MOF/SiNPs in the presence and absence of OTA (λ_{ex} = 395 nm, [OTA] = 500 ng/mL). (F) Fluorescence stability of Zr-MOF/SiNPs in 30 days.

sion peaks of Zr-MOF/SiNPs were presented at 450 and 650 nm. Once OTA was introduced, the emission intensity of Zr-MOF/SiNPs at 450 nm was greatly increased, along with red and violet photographs. Then we use sensor to perform fluorescence detection for 30 days to investigate its stability. The fluorescence intensity of Zr-MOF/SiNPs at 450 nm and at 650 nm showed minor change of its initial fluorescence after a month, confirming its superior potential as a fluorescence probe toward OTA detection (Fig. 2F). The excellent stability of Zr-MOF/SiNPs might come from the protection of SiNPs to Zr-MOF, which was utilized as an efficient fluorescence probe for OTA determination.

To get better analytical performance, the experimental parameters (such as the volume ratio of Zr-MOF/SiNPs, pH, reaction time and excitation wavelength) were optimized before applying the sensing system to OTA determination. It is of great significance to choose the appropriate excitation wavelength for fluorescence detection, and the trends of the fluorescence intensity ratio (I_{450}/I_{650}) with the excitation wavelength were monitored initially. In Fig. S4A (Supporting information), the maximum fluorescence response was obtained upon the excitation of 390 nm. Thus, 390 nm was selected for OTA detection in further work. According to the result in Fig. S4B (Supporting information), the FL intensity ratio I_{450}/I_{650} gradually increased with the volume of Zr-MOF increased from 0.5 to 2, and then reached a plateau, revealing that 1:2 volume ratio was sufficient for the OTA determination. Then, the fluorescent response of Zr-MOF/SiNPs toward OTA in different solvents were investigated. As shown in Fig. S4C (Supporting information), it can be found that the fluorescence response of Zr-MOF/SiNPs were greatly influenced by using different solvents. A maximum response toward OTA was obtained in the HEPES buffer. The effect of the pH of HEPES buffer in the range from 4.0 to 12.0 was explored. The maximum FL response was obtained when the pH was 10.0, which was directly chosen for further experiments (Fig. S4D in Supporting information). As illustrated in Fig. S5 (Supporting information), the reaction between Zr-MOF/SiNPs and OTA reached equilibrium in 1 min and remained steady until 10 min, which indicated that the interaction was rapid and efficiency. Consequently, 1 min was select as the optimum reaction time throughout the experiment.

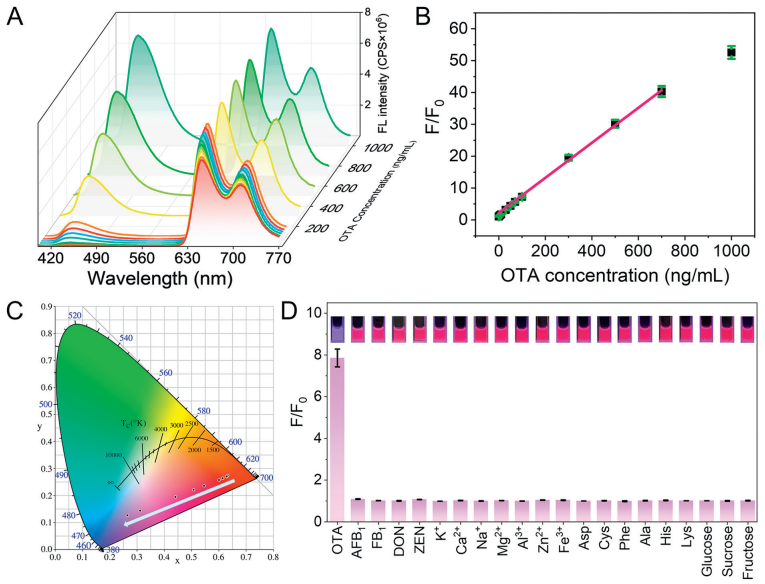

Fig. 3. (A) Emission spectra of Zr-MOF/SiNPs at different OTA concentrations. (B) The linear plot of the FL response of Zr-MOF/SiNPs *versus* different OTA concentrations, where F_0 and F are the FL intensity ratio (I_{450}/I_{650}) of Zr-MOF/SiNPs before and after addition of OTA. (C) The corresponding CIE chromaticity coordinates of Zr-MOF/SiNPs. (D) Fluorescence response of Zr-MOF/SiNPs to different substances (100 ng/mL) in the OTA detection (inset: corresponding fluorescence images of the samples under a 365 nm UV lamp).

Fluorescence spectrometric titration experiments were used to verify the potential of Zr-MOF/SiNPs as a fluorescent probe for OTA. As depicted in Fig. 3A, with an increase of the OTA concentration, the FL intensity at 450 nm increased sequentially. The fluorescence intensity ratio I_{450}/I_{650} displayed an excellent linear calibration to OTA concentrations between 0.05 ng/mL and 700 ng/mL ($R^2 = 0.998$, Fig. 3B). Due to the enrichment ability of Zr-MOF/SiNPs to OTA, the limit of detection (LOD) and limit of quantitation (LOQ) of the sensing platform to OTA was 0.016 ng/mL and 2.44 ng/mL, which is lower than Zr-MOF, SiNPs and most of existing methods showed in Table S1 (Supporting information). Meanwhile, the LOD is much lower than the permissible concentration in health foods and safe feeds (<5 ng/mL), demonstrating that this sensing platform would be a promising option for the OTA assay in food samples. In Fig. 3C, the obvious emission color shift could be clearly identified in CIE chromaticity diagram. With the addition of OTA, the fluorescent color of the sensing system gradually transformed from red to blue, implying the Zr-MOF/SiNPs could be applied as an efficient probe for the visual detection of OTA.

Different kinds of interferences [aflatoxin B_1 (AFB_1), fumonisin B_1 (FB_1), deoxynivalenol (DON), zearalenone (ZEN), K^+, Ca^{2+}, Na^+, Mg^{2+}, Al^{3+}, Zn^{2+}, Fe^{3+}, Asp, Cys, Phe, Ala, His, Lys, glucose, sucrose and fructose] were selected to evaluate the specificity and anti-interference ability of the above sensing platform. As shown in Fig. 3D, only OTA could cause a significant enhancement of I_{450}/I_{650} of the sensing system, exhibiting the excellent specificity of Zr-MOF/SiNPs for OTA detection. Then, the anti-interference ability of Zr-MOF/SiNPs was tested in the presence of similar mycotoxins (AFB_1, FB_1, DON, ZEN) and other interfering substance. When the potentially interfering substances coexisted with OTA in the system, it can be noticed that fluorescence responses were almost the same as those towards OTA (Fig. S6 in Supporting information). The above results verified that visual detection platform possessed high selectivity and anti-interference ability of the system to OTA.

To further evaluate the mechanism of the fluorescent behavior of OTA by Zr-MOF/SiNPs, the details of interaction between the sensor and OTA was investigated. At an excitation wavelength of 400 nm, the maximum emission peak of Zr-MOF was found at 650 nm. It had been reported that the fluorescence emission peak

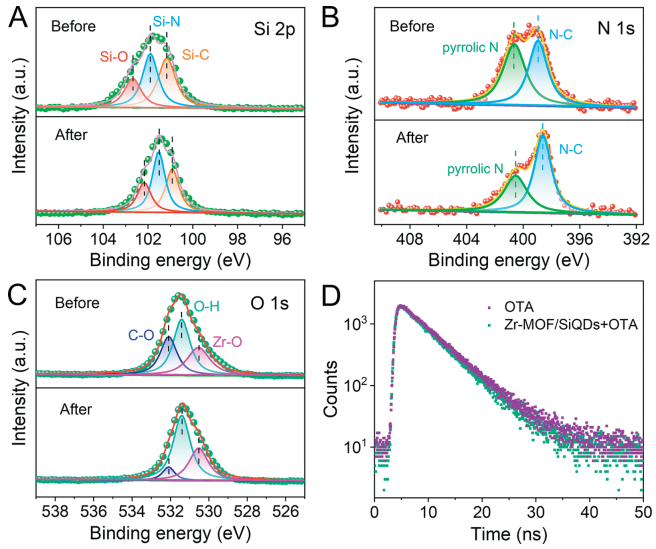

Fig. 4. XPS spectra of (A) Si 2p region, (B) N 1s region and (C) O 1s region of Zr-MOF/SiNPs before and after OTA addition. (D) Fluorescence lifetime of OTA and Zr-MOF/SiNPs+OTA at 450 nm (excited at 365 nm).

at 450 nm for OTA was produced by excitation at 380 nm in alkaline media [53]. And the formation of OTA/SiNPs further enhance the intrinsic fluorescence of OTA [54]. This outcome culminated in a ratiometric fluorescent response towards OTA, accompanied by a shift in emission color from red to blue. The coordination modes between OTA and Zr-MOF/SiNPs were described in Fig. S7 (Supporting information). The large conjugate structure of Zr-MOF and the Zr^{4+} and Si in Zr-MOF/SiNPs is available to form more stable $\pi-\pi$ coordination, and hydrogen bond with OTA. The XPS spectrum of Zr-MOF/SiNPs further revealed the formation of Zr-MOF/SiNPs. As shown in Fig. 4A, the XPS spectrum of Si 2p with peaks at 101.2, 101.8, and 102.6 eV corresponded to Si−C, Si−N, and Si−O, respectively. After combining with OTA, the relative amount of Si−N increased from 37.58% to 43.03% after OTA addi-

Table 1
Determination results of OTA in cereal samples.

Samples	Detected (ng/mL)	Spiked (ng/mL)	Found (ng/mL)	Recovery (%)	RSD (%)
Rice	No detected	5	5.13	102.7	1.5
		10	9.94	99.5	1.7
		50	42.83	85.7	4.1
Maize	No detected	5	4.54	90.8	2.6
		10	9.76	97.6	3.6
		50	48.58	97.2	1.1
Millet	No detected	5	4.84	96.8	1.6
		10	9.34	93.5	3.8
		50	47.69	95.4	1.3

tion, demonstrating that the possible noncovalent interactions between OTA and SiNPs, such as the N–H···N/O hydrogen interactions. In the N 1s spectrum of Zr-MOF/SiNPs depicted in Fig. 4B, there is a shift of N−C toward higher binding energy after interacting with OTA, and the content of N−C increases from 46.12% to 58.24%, which could be contributed to the formation of C−N−O bond between the C−N group of OTA and the Zr−O of Zr-MOF/SiNPs. The O 1s spectra of Zr-MOF/SiNPs shown in Fig. 4C revealed the existence of Zr−O (530.54 eV), O−H (531.42 eV) and C−O (530.54 eV) bonds. The relative amount of Zr−O increased from 28.60% to 32.15% after OTA addition, which might due to the formation of the surface complex between metal ions in Zr-MOF/SiNPs and oxygen elements in OTA. The relative amount of C−O bond decreased from 28.95% to 8.75%, which might be caused by the hydrogen bonding interaction between C−O in Zr-MOF/SiNPs and –NH–, –COOH in OTA. In addition, all these peaks of N 1s and O 1s shift to the higher binding energy, which may be contributed to $\pi-\pi$ stacking between OTA and Zr-MOF/SiNPs. In the present study, we observed a fluorescence lifetime shorten for Zr-MOF/SiNPs-OTA, whereas the complexation of OTA by the probe changed the ligand's fluorescence lifetime slightly (Fig. 4D). The TEM image of Zr-MOF/SiNPs-OTA were still consistent with that of Zr-MOF/SiNPs, confirming the structure of Zr-MOF/SiNPs was maintained stable (Fig. S8 in Supporting information). Consequently, the strong host–guest interaction and the intrinsic fluorescence of OTA upon binding with Zr-MOF/SiNPs can be firmly believed to be the reasons for the fluorescence turn-on sensing mechanism.

The smartphone was used to convert the color signal into RGB values to make the visual sensing platform of OTA more portable and accuracy. After capturing the fluorescence images, the OTA concentration can be evaluated *via* calculating the ratio of the red and blue channel values. As illustrated in Fig. S9 (Supporting information), the sensing platform showed obvious fluorescence color changes from red to blue, and the RGB values was extracted by FC Picker. The B/R value showed an excellent linear relationship with OTA concentration ($R^2 = 0.988$). The LOD of OTA was calculated to be 1.75 ng/mL, indicating smartphone has potential practicability for *in-situ* quantitative analysis of OTA.

Based on its excellent detection performance, the accuracy and reliability of Zr-MOF/SiNPs was further evaluated in a complex environment. Three different spiking levels (5, 10, 50 ng/mL) were applied to OTA determination in rice, maize, and millet samples. As list in Table 1, the average spiked recoveries were in the range of 85.7%–102.7% with a relative standard deviation (RSD) below 4.12%. Thus, these experimental results revealed the proposed probe has acceptable accuracy and precision of for OTA detection in real samples.

In summary, a label-free fluorescent sensing platform was developed by combining a smartphone-based reading system with Zr-MOF/SiNPs for rapid, reliable and sensitive determination of OTA. Due to the strong non-covalent force between the fluorescent probe and OTA, this sensing platform exhibited a low LOD and broad linear range for OTA determination. Meanwhile, the Zr-MOF/SiNPs sensor showed good specificity and strong anti-interference capability from other common mycotoxins. The smartphone was employed to convert the image color signal into RGB values to achieve the visual sensing for OTA, and the LOD for OTA was achieved as low as 1.75 ng/mL. Furthermore, the prepared Zr-MOF/SiNPs sensor has been successfully applied in OTA detection in maize samples with satisfactory recovery rate. This method not only provides a promising fluorescent sensing platform based on nanostructured porphyrinic metal organic frameworks, but also offers a new sight for accurate OTA determination away from the assistant of biomaterials.

Declaration of competing interest

The authors declare that there is no conflict of interest.

CRediT authorship contribution statement

Yijian Zhao: Conceptualization, Formal analysis, Methodology, Writing – original draft. **Jvzhe Li:** Conceptualization, Methodology. **Yunyi Shi:** Formal analysis, Investigation. **Jie Hu:** Formal analysis, Investigation. **Meiyi Liu:** Validation, Visualization. **Yao Shen:** Validation, Visualization. **Xinglin Hou:** Validation, Visualization. **Qiuyue Wang:** Validation, Visualization. **Qi Wang:** Validation, Visualization. **Zhiyi Yao:** Conceptualization, Funding acquisition, Project administration, Supervision, Writing – review & editing.

Acknowledgments

Z. Yao received funding from the National Natural Science Foundation of China (No. 31871877) and the National Key Research and Development Program of China (No. 2019YFC1606303).

Supplementary materials

Supplementary material associated with this article can be found, in the online version, at doi:10.1016/j.cclet.2024.110132.

References

[1] B. Wang, Y. Wu, Y. Chen, et al., Biosens. Bioelectron. 81 (2016) 125–130.
[2] Y. Hou, N. Long, Q. Xu, et al., Food Chem. 403 (2023) 134375.
[3] X. Huang, S. Zhan, H. Xu, et al., Nanoscale 8 (2016) 9390–9397.
[4] L. Wei, Z. Wang, Y. Chen, J. Agric. Food Chem. 70 (2022) 14798–14804.
[5] W. Li, X. Zhang, X. Hu, et al., ACS Appl. Mater. Interfaces 14 (2022) 5615–5623.
[6] Y. Hou, B. Jia, P. Sheng, et al., Compr. Rev. Food. Sci. Food Saf. 21 (2022) 2032–2073.
[7] M. Qiao, M. Liu, Z. Wan, et al., Microchim. Acta 190 (2023) 313.
[8] H. Yan, L. Zhang, Z. Ye, et al., J. Agric. Food Chem. 69 (2021) 12021–12029.
[9] X. Zhang, Z. Cheng, L. Ma, J. Li, Food Chem. 227 (2017) 55–63.
[10] Y. Zhang, L. Wang, X. Shen, et al., J. Agric. Food Chem. 65 (2017) 4830–4838.
[11] X.B. Huang, S.H. Wu, H.C. Hu, J.J. Sun, ACS Sens. 5 (2020) 2636–2643.
[12] H. Guo, P. Ma, K. Li, et al., Sens. Actuator B: Chem. 358 (2022) 131484.
[13] L. Liu, J. Jiang, G. Liu, et al., ACS Appl. Mater. Interfaces 13 (2021) 35997–36010.
[14] M.M. Chen, M.L. Zhang, X. Song, et al., Chin. Chem. Lett. 36 (2025) 109785.
[15] Z. Chen, J. Ma, D.W. Sun, Compr. Rev. Food. Sci. Food Saf. 22 (2023) 2977–3010.
[16] X. Miao, C. Wu, F. Li, M. Zhang, Adv. Funct. Mater. 33 (2023) 2212980.
[17] L. Zeng, Y. Ke, X. Yang, et al., Food Chem. 438 (2024) 138044.
[18] H. Ye, S. Koo, Z. Beitong, et al., Anal. Chem. 94 (2022) 15423–15432.
[19] S.M. Tawfik, M. Sharipov, S. Kakhkhorov, M.R. Elmasry, Y.I. Lee, Adv. Sci. 6 (2019) 1801467.
[20] L. Wang, L. Wen, Y. Chen, F. Wang, C. Li, Chemosphere 304 (2022) 135405.
[21] M. Xiao, Z. Liu, N. Xu, et al., ACS Sens. 5 (2020) 870–878.
[22] Y. Li, B.L. Chai, H. Xu, et al., Inorg. Chem. Front. 9 (2022) 1504–1513.
[23] S. Wang, Y. Zhang, G. Pang, Y. Zhang, S. Guo, Anal. Chem. 89 (2017) 1704–1709.
[24] X. Lin, C. Li, C. He, et al., ACS Appl. Nano Mater. 4 (2021) 8231–8240.
[25] H. Wang, B. Zhao, Y. Ye, et al., Biosens. Bioelectron. 207 (2022) 114164.
[26] K. Wang, Y.L. Zhu, T.F. Zheng, et al., Anal. Chem. 95 (2023) 4992–4999.
[27] Y. Zhao, T. Liu, J. Gao, et al., Anal. Chem. 95 (2023) 8250–8257.
[28] A.G. Ayankojo, J. Reut, A. Öpik, A. Furchner, V. Syritski, Biosens. Bioelectron. 118 (2018) 102–107.

[29] N. Katumo, G. Gao, F. Laufer, B.S. Richards, I.A. Howard, Adv. Opt. Mater. 8 (2020) 2000507.
[30] L. Zhao, W. Wang, Y. Wang, et al., J. Hazard. Mater. 417 (2021) 125986.
[31] Y. Zhang, X. Zhu, M. Li, H. Liu, B. Sun, J. Agric. Food Chem. 70 (2022) 6059–6071.
[32] Z. Chen, Y.L. Lu, L. Wang, et al., J. Am. Chem. Soc. 145 (2023) 260–267.
[33] X. Dou, G. Wu, Z. Ding, J. Xie, Food Chem. 416 (2023) 135805.
[34] M. Zhang, X. Guo, Trends Food Sci. Technol. 129 (2022) 621–633.
[35] L. Guo, M. Wang, D. Cao, Small 14 (2018) 1703822.
[36] Z. Han, K. Wang, H.C. Zhou, P. Cheng, W. Shi, Nat. Protoc. 18 (2023) 1621–1640.
[37] L. Qin, J. Cao, D. Lin, et al., Chem. Eng. J. 464 (2023) 142550.
[38] J. Chen, F. Xu, Q. Zhang, S. Li, X. Lu, Analyst 146 (2021) 6883–6892.
[39] Z. Han, K. Wang, Y. Chen, et al., CCS Chem. 4 (2022) 3238–3245.
[40] D. Chen, W. Liu, Z. Guo, et al., Inorg. Chem. 60 (2021) 18133–18140.
[41] D.Y. Zheng, E.X. Chen, C.R. Ye, X.C. Huang, J. Mater. Chem. A 7 (2019) 22084–22091.
[42] F. Wang, Z. Li, H. Jia, et al., Food Chem. 383 (2022) 132389.
[43] B. Mohan, G.S. Priyanka, et al., J. Hazard. Mater. 453 (2023) 131324.
[44] S. Xing, C. Janiak, Chem. Commun. 56 (2020) 12290–12306.
[45] M. Zhan, S. Hussain, T.S. AlGarni, et al., Mater. Res. Bull. 136 (2021) 111133.
[46] M. Wang, X. Meng, N. Liu, et al., Chin. Chem. Lett. 34 (2023) 107995.
[47] W. Zhou, J. Zhu, D. Fan, et al., Adv. Funct. Mater. 27 (2017) 1704092.
[48] Q. Wang, Q. Tan, S. Zhao, et al., Chem. Eng. J. 470 (2023) 144061.
[49] L. Zeng, X. Xiao, H. Ye, D. Ma, J. Zhou, Food Chem. 394 (2022) 133489.
[50] W. Liu, Y.M. Wang, Y.H. Li, et al., Small 13 (2017) 1603459.
[51] S. Yao, H. Xu, T. Zheng, et al., Chin. Chem. Lett. 34 (2023) 107532.
[52] S.D. Doke, C.M. Patel, V.N. Lad, Silicon 14 (2022) 913–922.
[53] Z. Tang, X. Liu, Y. Wang, et al., Environ. Pollut. 251 (2019) 238–245.
[54] M. Zhang, S. Zhang, X. Guo, et al., J. Hazard. Mater. 465 (2024) 133104.